Arabian Journal of Geosciences (2020) 13: 19
https://doi.org/10.1007/s12517-019-5017-5

ORIGINAL PAPER

Integrated use of electrical resistivity tomography and ground penetration radar for identifying subsurface sinkholes in Rufa Graben, Central Riyadh

Saad Mogren[1]

Received: 14 March 2019 / Accepted: 6 December 2019 / Published online: 23 December 2019

Abstract
Two-dimensional electric resistivity tomography and ground-penetrating radar (GPR) study was carried out in the eastern Rufa Graben, Riyadh area. Dipole–dipole configuration was used with a total length of 360 m and an electrode spacing of 5 m. In addition, the same number of ground-penetrating radar profiles was conducted in the same location of the electrical resistivity tomography (ERT) profiles. The goal of this study was to map and delineate the subsurface karstic features in the study area such as sinkholes, cavities, and fractured zones. The two methods showed the efficiency to detect the near-surface cavities and their distribution in the study area. The detected cavities were of different sizes. The air-filled cavities have appeared in ERT sections as anomalies that have high resistivity values while the cavities filled with wet clay were characterized with low-resistivity values. In GPR sections, the karstic features were seen by either hyperbola diffractions or uplift and discontinuity in horizontal reflection events. The results obtained from this study will contribute in solving the geotechnical problems for any expected future constructions planned to be done in the study area.

Keywords Rufa Graben · ERT · GPR · Sinkholes · Karst

Introduction

The unconsolidated and sedimentary rocks cover the center portion of the Kingdom of Saudi Arabia. Most of rocks in this part are of carbonate nature including limestone, dolomite, and evaporites (Powers et al. 1966). Those rocks are affected by the existence of karstic features such as sinkholes, karrens, domepits, grottos, or deeply incised canyon-like valleys. Karstic features in the central part of Saudi Arabia are known for their typical morphology as well as source for potential aquifers as cited in *Global Karst Datasets* (Hollingsworth et al. 2008). Such karstic aquifers are particularly vulnerable to both pollution from surface activities and large-scale dewatering from limestone mining operations. This is because of the enhanced vertical and lateral flow paths, resulting from the dissolution of carbonate species by surface water runoff as well as the rainfall. Often these processes result in the development of voids that can range in size up to several tens of meters. Physiographic features like cliffs, geologic boundaries, faults, or fault-bounded graben also play an important role in developing the karstic features. The City of Riyadh is characterized by the presence of these features along the Tuwaiq plateau and further east toward Al-Kharj in the Ar-Riyadh area. Dangerous geohazards problems can affect the environment and infrastructures due to the existence of underground cavities and voids in the near-subsurface limestone (Sum et al. 1996). The risk of unexpected development of sinkholes in karst areas has negative results and repercussions on foundations and land used for agriculture (Parise and Gunn 2007).

For many years ago, karst geohazards such as cavities, weathered zones, and sinkholes have been investigated using several geophysical tools. The obvious contrast between the cavities filled with air or sediment, on the one hand, and the host rock, on the other hand, has helped the geophysical techniques to be applied successfully in karst landforms. The tools used for studying karst hazards mapping contain gravity (Amrouche and Saibi 2019; Saibi et al. 2019; Saibi and Amrouche 2018), magnetometry, ground-penetrating radar (Pueyo-Anchuela et al. 2010), seismic reflection (Cook 1965), and DC resistivity tomography (Abu-Shariah 2009; Deceuster et al. 2006).

Responsible Editor: Li Zhen Cheng

✉ Saad Mogren
smogren@ksu.edu.sa

[1] Department of Geology and Geophysics, College of Science, King Saud University, Riyadh 11451, Saudi Arabia

The present work has been achieved to study the configuration of subsurface sinkholes in the eastern part of Rufa Graben and their continuous extension of underneath fractures and to evaluate their dangers affecting people and land use. The importance of this study lies in detecting the locations of subsurface sinkholes in the study area where this area considered an extension to the urban ones in which many prominent projects are going to be done as mentioned in the "Introduction."

The ability of locating these sinkholes by electrical resistivity tomography (ERT) and ground-penetrating radar (GPR) methods before starting any urban projects plays a very important role in avoiding the undesirable or dire consequences of either loss of lives or economic losses. This protective procedure is represented by injecting subsurface empty sinkholes by cement to prevent subsidence in the future when a load is applied to the surface above these sinkholes.

Metwaly and AlFouzan (2013) studied the existence of cavities in the eastern part of Saudi Arabia using two-dimensional geoelectrical resistivity tomography. The method could determine the extension of shallow weathered zones and locate different sizes of cavities underneath them.

An integrated study using remote sensing and ERT methods was successfully employed to detect the old sinkholes in the An Nu'ayriyah area, southwest of Al Khafji City (Youssef et al. 2012).

Jado and Johnson (1983) explored two considerable solution cavities in the Ad Dammam Dome; one of these cavities appeared during the central library construction in the King Fahd University of Petroleum and Minerals (KFUPM). Globally, a recent study by Carbonel et al. (2015) used multiple techniques including ERT and GPR. The ERT section collected in the Vistabella Park definitely images the graben structure detected on the western margin of the northern sinkhole. The great conductivity existing in the study area has affected negatively the results obtained; however, some profiles refer that the depressions in the study area is related to sagging.

Yassin et al. (2014) used six ERT profiles along two housing-complicated construction places, north of Ipoh City, in the Perak State, Peninsular Malaysia, to investigate the karstic issues like voids, channels, and cavities. The results referred to the presence of anomalies with a low degree of resistivity along the study area. Moreover, the study could predict if a collapse can happen in the near future.

Study area description

Geomorphology

The study area (Fig. 1) is located between 24.25° and 24.40° of latitude and 47.00° to 47.25° of longitude approximately 40 km to the southeast of Riyadh near the Riyadh–Al-Kharj Highway. The study area height varies from 360 m above mean sea level (amsl) to 595 m amsl with an average elevation of 481.5 m. The Jibal Jubayl escarpment runs in a northwest–southeast direction and is in the north of the study area. It is followed by the Maraghah depression to the south. South of the Maraghah depression, elevated portion corresponds to the Jibal Umm Ash Shal. It is followed by the Rufa Graben, and south of the Rufa Graben is the Wadi Hanifa trending in a northwest–southeast direction.

Geology

The Rufa Graben name is derived from the name of the Ar Rufa village placed to the east of the graben. The graben location is the southeast of Riyadh Quadrangle which is covered by Phanerozoic sedimentary rocks of the western edge of the Arabian platform, which is a place over Proterozoic basement at an estimated depth range between 5 and 8 km (Phoenix 1985).

Four kilometers long and 800 m wide, the Ammaj segment of the Rufa Graben forms a trough striking 085°, characterized by a vertical throw of between 20 and 30 m, and bounded by two parallel flexures that affect collapsed Sulaiy Formation rocks (Fig. 2). The bottom of the graben is filled with surficial deposits from which outcrops of Sulaiy Formation emerge, together with some outcrops of Sha'al Formation. The north edge of the Sha'al segment is formed by large progressive east–west-trending flexures arranged en echelon and cut by normal and reverse faults. These flexures affect the collapsed Sulaiy Formation and the outliers of conformable Yamama and Buwaib Formation rocks. The Rufa Formation, which lies horizontally unconformably on the abovementioned formations, is not affected by the faults but tends to be affected by the flexures (as indicated by the southward dips).

The south edge of the graben is reduced to a thin horst of Sulaiy Formation rocks. The flexured and faulted south flank of this horst is interpreted as the north edge of a small, unnamed southern graben running parallel to the Rufa Graben. The only outlier visible at the bottom of this graben structure, otherwise entirely masked by dunes, consists of Yamama Formation rocks capped by the Rufa Formation. Outliers of Rufa Formation are affected by this flexuring, and one is offset 16 m vertically by a normal fault. The eastern extremity of the Ashqar Maraghah segment shows the Sha'al and Rufa Formations buried under surficial deposits, and the structure of this extremity, together with the southward extension of the Rufa Graben, is therefore not visible in outcrop (Vaslet et al. 1991).

The Rufa Graben comprises of geological formations ranging from Early Cretaceous to the Quaternary as shown in Table 1 The main formations exposed include the Sulay, Yamama, Biyadh, Aruma, Ummer Radhuma, and Kharj Formations. The Quaternary period is represented by the unconsolidated surficial deposits. In the study area, only two formations appeared on the surface: Arab and Sulay Formations (Fig. 3).

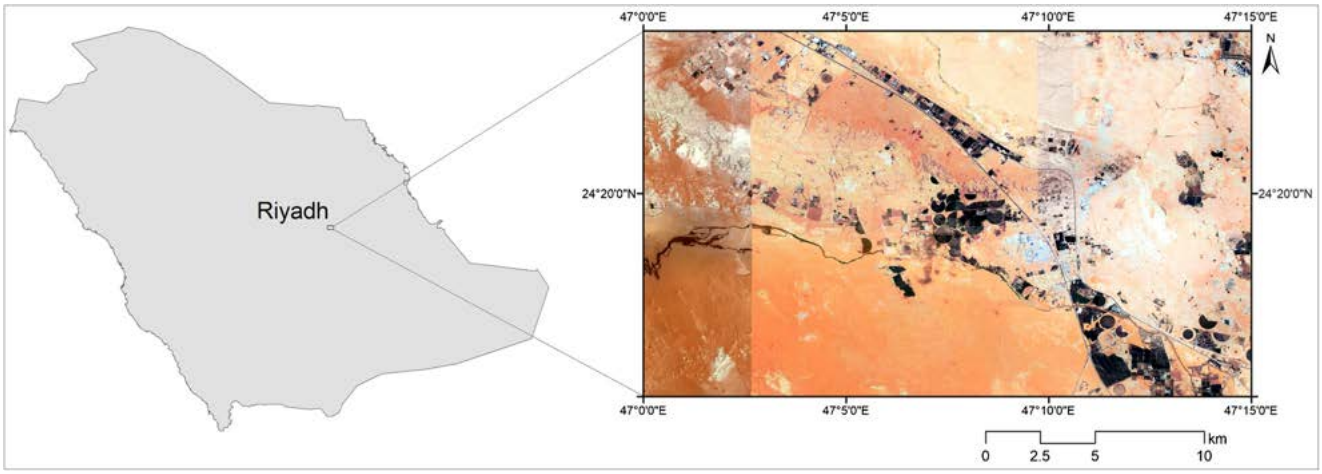

Fig. 1 Satellite image of the study area

Methodology

The application of geophysical techniques in karst zones has been of high importance in the last two decades due to the rapidly growth in technology in addition to decreasing in the cost of data acquisition, processing and interpretation. The importance of mapping the near surface karst features like voids, cavities, tunnels and sinkholes has a strong relationship with engineering and environmental works (Chalikakis et al. 2011).

ERT survey

Due to the limitation of the VES and HEP as they measure only the variations in resistivity of the subsurface horizontally

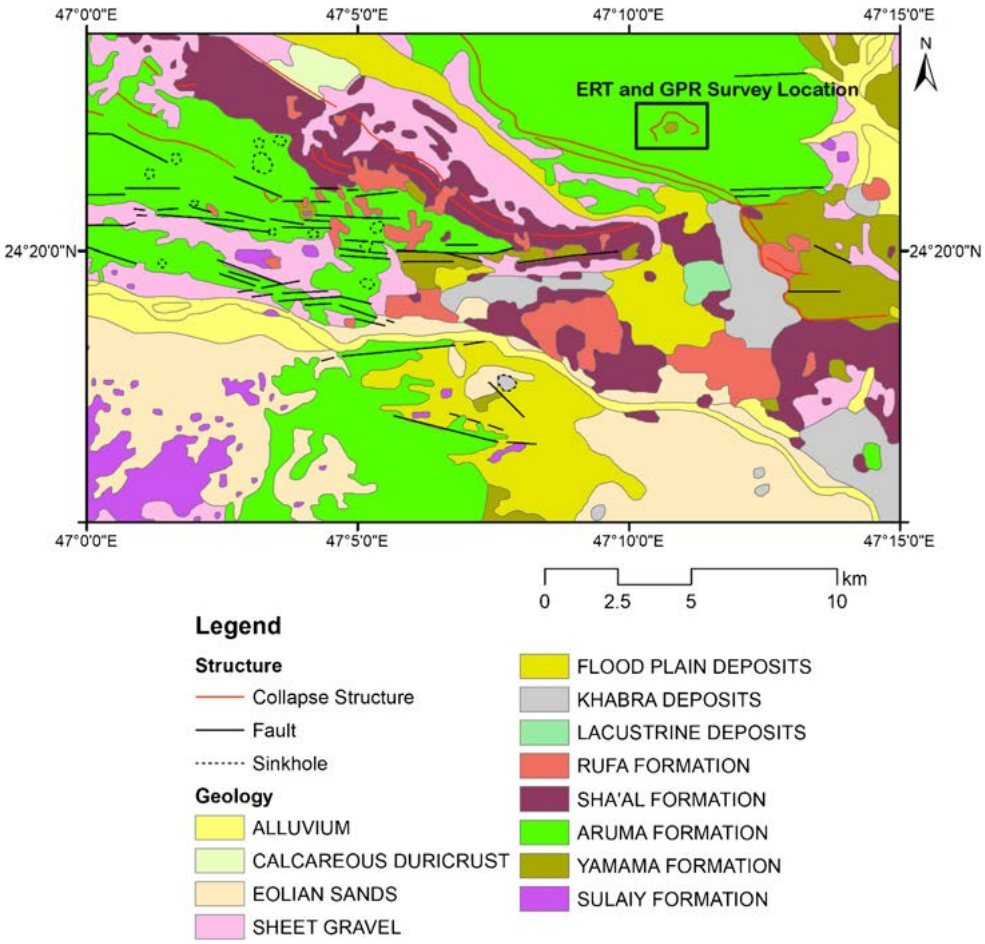

Fig. 2 Geology of the study area

Table 1 Lithostratigraphic column of the study area (Vaslet et al. 1991)

Formation	Period	Lithology
Quaternary surficial deposits	Quaternary	Silt, gravel, and unconsolidated silt and gravel
Ummer Radhuma	Paleocene	Limestone, dolomitic limestone, dolomite
Aruma	Late Cretaceous	Limestone and some dolomite, shale, lower sands in NW and south
Biyadh	Middle Cretaceous	Sandstone, subordinate shale, rare dolomite lenses
Yamama	Early Cretaceous	Calcarenitic rocks, aphanitic limestone, calcarenite
Sulaiy	Early Cretaceous	Limestone, chalky aphanitic calcareous limestone

and vertically independently, a new technique called two-dimensional (2-D) is developed to deal with this deficiency. In this method, a more precise imaging of the subsurface is defined by a model where the resistivity distribution in both the two vertical and horizontal directions along the survey line is measured. This technique has the ability to obtain about 100 to 1000 measurements at once according to the number of electrodes used in the survey. That means that the 2-D survey design is more rapid in the data acquisition in comparison to the 1-D survey, but it is more expensive. It is useful to use this technique in conjunction with GPR or seismic surveys to give complementary details about the subsurface. Nowadays, the ERT technique is considered the most effective and practical as it has the ability to produce a detailed image of the subsurface with a minimum cost and time (Loke 2002). Different electrode configurations such as Wenner configuration, Schlumberger configuration, and dipole–dipole configuration can be used in carrying out the ERT survey. In the present study, the dipole–dipole configuration was used.

In this array (Fig. 4), the spacing between the current electrode pair (A–B) and the potential electrode pair (M–N) is the same and is given as "*a*." This array has another factor marked as "*n*" representing the ratio of the distance between the B and M electrodes to the A–B (or M–N) dipole separation *a*. The apparent resistivity in this array is calculated from this equation

$$\rho a = \frac{V}{I}\pi an(n+1)(n+2) \tag{1}$$

When this array is used in a survey, the *a* spacing is initially kept fixed and the *n* factor is increased from 1 to 2 to 3 until up to about 6 in order to increase the depth of investigation.

The sensitivity function plot in Fig. 4 shows that the largest sensitivity values are located between the A and B dipole pair, as well as between the M and N pair. This means that this array is most sensitive to resistivity changes between the electrodes in each dipole pair. It could be noticed that the sensitivity contour pattern is almost vertical.

Thus, the dipole–dipole array is very sensitive to horizontal changes in resistivity, but relatively insensitive to vertical changes in the resistivity. That means that it is good in mapping vertical structures, such as dykes and cavities, but relatively poor in mapping horizontal structures such as sills or sedimentary layers. One possible disadvantage of this array is the very small signal strength for large values of the *n* factor which can be solved by increasing the *a* spacing between the C1 and C2 (and P1–P2) dipole pair to reduce the drop in the

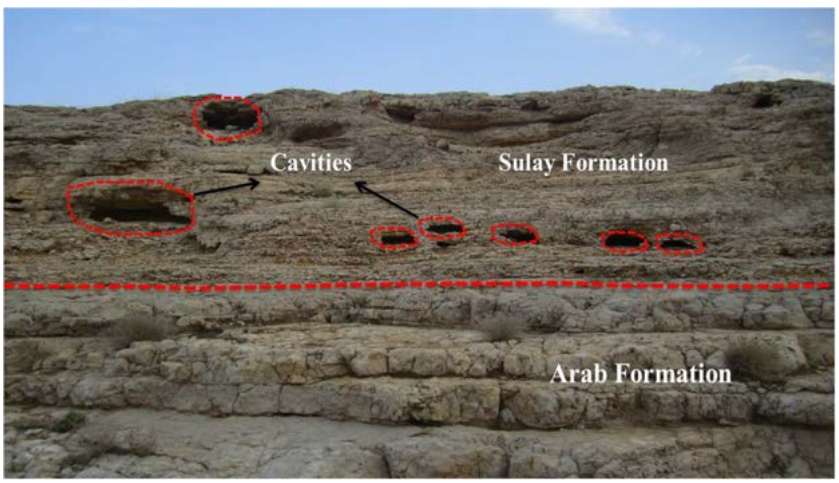

Fig. 3 Field photograph showing the surface geology of the study area

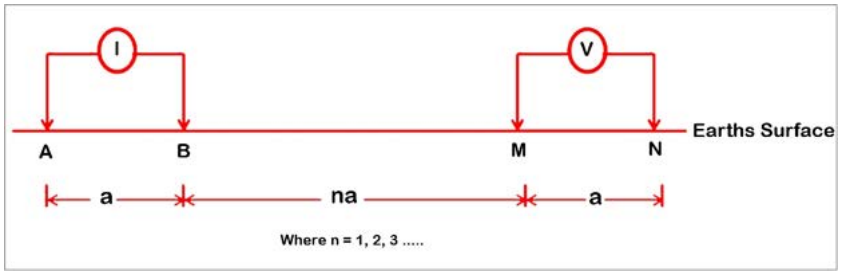

Fig. 4 Arrangement of the dipole–dipole array

potential when the overall length of the array is increased to increase the depth of investigation. This array was conducted in our study. It is considered the most effective and non-expensive configuration in delineating areas of karst hazards and in imaging the sinkhole collapse area (Zhou et al. 2002).

GPR survey

The phrase ground-penetrating radar is commonly used to describe a series of electromagnetic methods developed basically for determining and mapping subsurface objects and border structure (Daniels 2004). GPR has been applied widely in geophysical investigations as it is considered a non-intrusive and high-resolution method. It is generally used in detecting the depth, thickness, and extension of underground anomalies in zones where conductivity is very low (Wilson and Beck 1988).

The system of GPR is formed from a few components, as can be clarified in Fig. 5. A source for editing electromagnetic wave (transmitter) is used. Another receiver is used to register the response from the subsurface. When a variation in dielectric properties or an anomaly with different electrical responses from the host rock is met, a reflected electromagnetic wave will be recorded at the receiver. This process is repeated to gather data at different locations along a profile. The final output can be represented by plotting the obtained signal amplitude against time and position to finally give an image of vertical subsurface. The depth of penetration can be calculated by determining the velocity of electromagnetic wave to convert the axis of time (Takahashi et al. 2012).

The attenuation of the GPR signal energy is affected by distribution of the subsurface electrical resistivity and the dielectric constant. Those properties are influenced by the degree of moisture and the percentage of porosity in the host subsurface materials.

The relation between velocities of the radar signal and the relative permittivity can be calculated from this equation

$$v = \frac{c}{\sqrt{(\mu r \varepsilon r)}} \tag{2}$$

where $\epsilon r = \frac{\epsilon}{\varepsilon 0}$ is the ratio of the dielectric permittivity of the medium to the dielectric permittivity of free space, $\mu r = \frac{\mu}{\mu 0}$ is the relative magnetic permeability of the medium, and $c = 3 \cdot 10^8$ m/s is a constant of the speed of EM waves in free space.

While μr is near to unity for most rock materials, radar speed is primarily controlled by ϵr (Davis and Annan 1989).

Geophysical Surveys Systems, Inc., in its SIR-2000 user's manual 2011 tabulates dielectric constants for common materials. Those dielectric constants are shown in Table 2.

When information about subsurface is not available or the material is suspected not to be homogeneous, the dielectric constant of the material can be precisely calculated, knowing the depth of an object immersed in the same material and the two-way travel time. The final measured data is displayed on a graph called diagram plot of distance versus time.

Field investigation

Six ERT and GPR surveys were carried out in the study area (Fig. 6). Each profile has a total length of 360 m. The six profiles were carried out in different directions in a trial to cover most of the study area, taking into consideration the accessibility to carry out the data acquisition. The 2-D ERT data have been picked up through the six profiles using multi-electrode system of Syscal Pro instrument which was equipped with external battery and multi-electrode cable with 72 electrodes. The resistivity data collected along the six ERT profiles were processed according to the following steps: data transfer, editing, and modeling.

After the data was collected in the field, it was transferred from the Syscal Pro instrument to Pc through the Prosys II software. Res2Dinv software (Loke 2000) was used for the data modeling. This software is designed for 2-D data inversion goals. The inversion method in the software depends on dividing the subsurface model into several numbers of rectangular blocks as shown in Fig. 7. The Res2Dinv software provides two main methods of inversion: the conventional least squares method and the robust inversion method. In the conventional least squares method, the square of difference between the measured and calculated apparent resistivity values is reduced. This method can give good results in case the data includes random or *Gaussian* noise. In the robust method, the absolute difference between the measured and calculated apparent resistivity values is reduced. The final one is used in

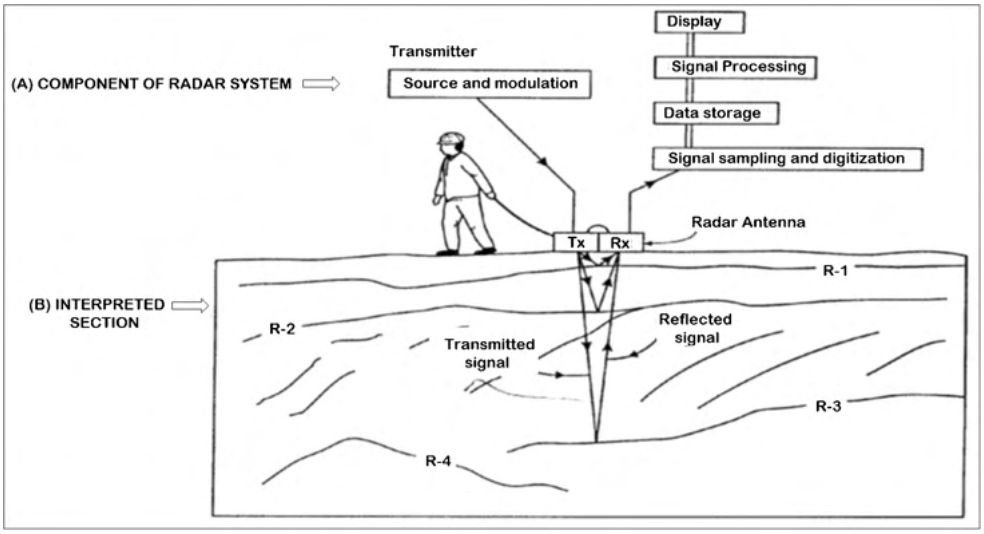

Fig. 5 Block diagram of a GPR system (Reynolds 2011)

case sharp boundaries could be faced in the subsurface (Claerbout and Muir 1973). In our study, we have chosen the robust inversion method after doing the synthetic model.

GPR profiles had a total length of 360 m. The position of these profiles is nearly in the same place of ERT profiles. The GPR technique is applied at the study area, east of Rufa Graben, to detect the subsurface sinkhole karst features. The GPR SIR 3000 system was used equipped with 400 MHz to image the subsurface with an expected depth of 3 m. The data were collected using the survey wheel, which enables distance measuring mode for the GPR system. The collected data had a trace spacing of 2 cm and 512 samples per trace. The GPR data were collected at a sampling rate of 50 scans per m. During the data acquisition, the data were filtered to weaken the noise and remove the effects of electromagnetic interference.

The main goal of applying the signal processes to the obtained subsurface ground-penetrating data is to get the most appropriate image which can readily be interpreted by the operator (Daniels 2004). The GPR data processing can be classified into two stages: basic and complicated. In our study, only the basic process step will be applied. The software Reflex 6.0 (Sandmeier 1998) was used for the data processing in our study. The process steps in this work include the time cut, background removal, band pass frequency, and automatic gain control.

Table 2 Dielectric value for common materials

Material	Dielectric constant	Velocity (mm/ns)
Air	1	300
Water (fresh)	81	33
Water (sea)	81	33
Polar snow	1.4–3	194–252
Polar ice	3–3.15	168
Sand (dry)	3–6	120–170
Sand (wet)	25–30	55–60
Silt (wet)	10	95
Clay (wet)	8–15	86–110
Clay soil (dry)	3	173
Limestone	7–9	100–113
Sandstone (wet)	6	112
Concrete	6–8	55–112
Asphalt	3–5	134–173

Result and discussion

ERT data

After all the six ERT lines were processed and modeled, these lines are going to be analyzed, taking into consideration the available geological data.

Geologic inference drawn from resistivity surveys must be done with a lot of considerations such as geologic information of the area under study, external features at the site, and reviewing similar work by other authors as there is no fixed resistivity for soils and rocks of the Earth's crust. These general concepts are important in the interpretation of the ERT data. Accordingly, the interpretation of the ERT data is done using the ranges of resistivity values of four common karstic limestones and its subsurface conditions, such as clayey content, fracturing and water content, and air-filled/clay-filled cavities. The karstic cavities in the limestone terranes create a quantifiable disturbance in the electrical conductivity with a

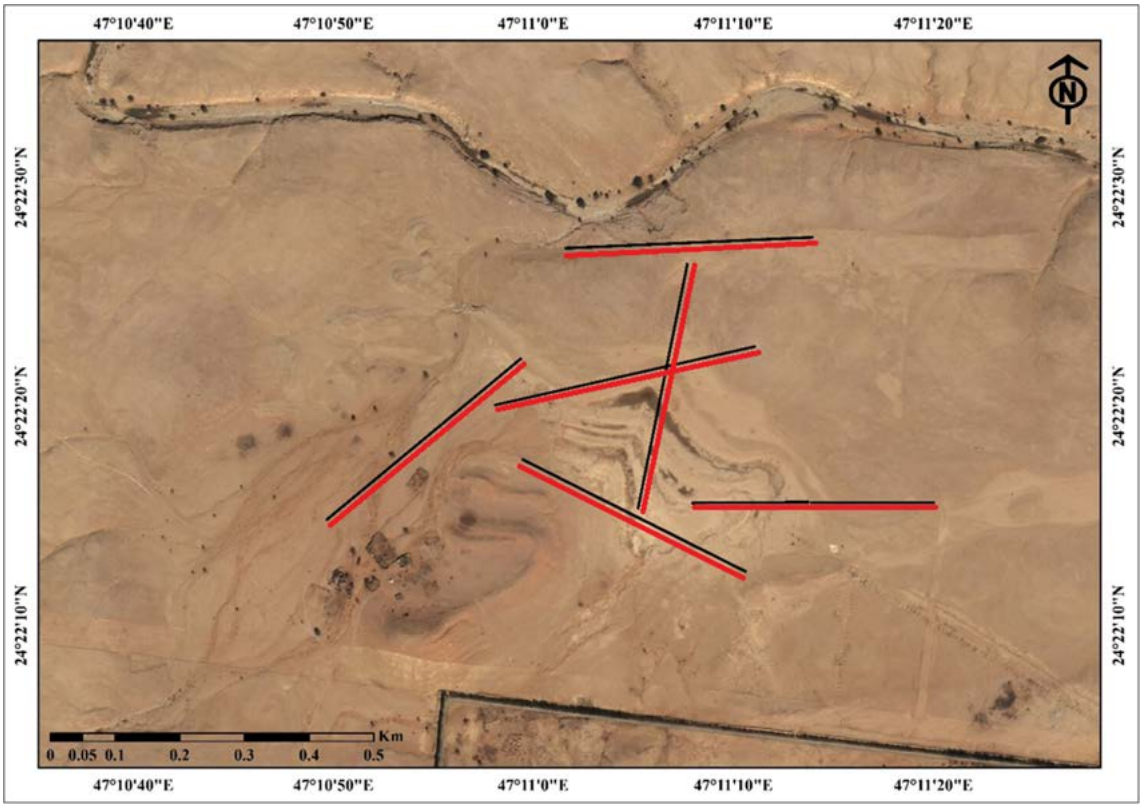

Fig. 6 A sketch showing the ERT (black lines) and GPR (red lines) profile locations in the study area

magnitude directly proportional to the filling material, degree of fracturing, and degree of weathering.

Based on the above facts and the geologic implications of the range of resistivity values obtained from the 2-D apparent resistivity model sections (Table 3, Fig. 7), the processed 2-D resistivity model sections are interpreted and explained in the following section.

GPR data

After the GPR data processing procedures were applied as mentioned previously, the interpretations of the 400 MHz profiles were carried out on the basis of horizontal variations and appearance of reflections. These variations and changes include strength, continuousness, and attenuation and lateral relations. Each of the abovementioned features refers to a special case. For example, the existence of a conductive zone such as sediment-filled cavity or water-saturated formation will be reflected as an attenuated area on the georadar section. The air-field cavities can be characterized on the georadar sections through following or tracing the laterally restricted series associated with large-amplitude pulses (Ulriksen 1982; Reynolds 2011). Losing of coherency or continuity and bending and scattering of reflections are also considered indicators for the existence of karstic features. The vertical and subvertical fractures can be seen on the georadar sections as discontinuities or displacements of reflection events in the horizontal direction (Grandjean and Gourry 1996; Grasmueck 1996).

Rufa 1 ERT profile

This ERT profile was measured between 24° 22′ 27.9″ and 24° 22′ 27.2″ of latitude and 47° 11′ 14″ and 47° 11′ 1.55″ of longitude, taking direction from west to east. Figure 8 shows the interpreted section of this profile. The Abs in this line is 6.1%. A layer of limestone (bordered with black dashed line) with a resistivity value ranging from nearly 1000 Ω·m to 1700 Ω·m could be delineated in the first 15 m containing different features of karsts. In the western part between offsets 45 m and 63 m with a depth between 6 and 12 m, an anomaly with high resistivity value interpreted as an air-filled cavity is determined.

Between offsets 80 m and 120 m, three interconnected cavities with a resistivity value of more than 1700 Ω·m reflect air-filled cavities with a depth ranging from 3 to 12 m. To the east of the center of the profile, three high-resistivity anomalies are delineated, referring also to the existence of air-filled cavities. Under this layer comes a new layer with a lower resistivity range representing a fractured limestone saturated with water especially in the lower western part of the profile.

Table 3 Geologic interpretation of the resistivity values obtained in this work

Geologic material	Description	Resistivity in Ω·m
Air-filled cavity	Very high resistivity that could vary depending on the conductivity on the depth/size/shape of cavity	> 1800
Wet clay–filled cavities	Very low resistivity that could vary based on the degree of saturation, porosity, and clay content	≤ 100
Fractured limestone	Moderate resistivity that could vary based on the degree of fracturing and clay intercalations	350–1000
Water-bearing fractured limestone	Very low resistivity that could vary based on the degree of fracturing and clay intercalations	≤ 150
Hard and massive limestone	Higher resistivity that could vary based on the degree of weathering and fracturing	> 2000

Rufa 1 GPR profile

This profile was conducted along the ERT profile Rufa 1 taking the same direction from west to east. In this section, different karst features could be determined at different depths. A very clear uplift and break or cutoff in reflection actions are detected between 110 and 125 m horizontal distances and extend to about 1.3 m in depth (Fig. 9a). This action refers to the existence of a cavity.

At about 90 m horizontal distance, a small diffraction hyperbola is detected and it may reveal the existence of a cavity. The same diffraction hyperbola is repeated at about 198 m horizontal distance but with an increasing depth to about 8 m.

Distortion and the absence of coherency which are indexes for the existence of karstic features such cavities or sinkholes could be mapped at a depth between 1 and 2 m along the 325 m and 348 m horizontal distances, respectively. The intensity of strong reflection events is very clear in the section (black dashed rectangular). This zone of intensity is associated with a fracture (the black vertical dashed line) indicated from discontinuity and displacement of horizontal reflections. In addition to this, another anomaly associated with a vertical open fracture is located between 1 and 2 m vertical depths and between 150 and 160 m horizontal distances (Fig. 9b).

Rufa 2 ERT profile

This profile is measured in the direction southwest to northeast which is nearly parallel to line 1. The upper northern west part of the profile is covered by very moist fractured limestone distinguished with low resistivity value as shown in Fig. 10. In this profile, a zone of the limestone formation marked by a black dashed line and high-resistivity different size cavities with a depth range from 2 to 10 m is recognized. In the first part of the section between offset 65 m to 85 m and offset 117 m to 147 m, two air-filled cavities with a maximum depth of 4 m and 8 m, respectively, could be determined. A third high-resistivity anomaly referring to an air-filled cavity is located between offsets 215 m and 228 m.

Rufa 2 GPR profile

This profile was carried out along the same path of the Rufa 2 ERT profile taking direction from southwest to northeast. These radiograms (Fig. 11a, b) contain numerous karst features. In the first part (Fig. 14) of this section, a small diffraction hyperbola (its apex located at 68 m horizontal distance) could be delineated at a depth of more than 3 m and extend deeper to the end of the section. Another diffraction hyperbola could also be mapped in the shallow part of this section between 170 and 180 m horizontal distances, and its apex starts at 0.3 m depth. Distortion, discontinuity, and intensity of the reflection signal could be seen in this section between 1 and 2 m vertical depths at a horizontal distance of 18–24 m, 45–52 m, and 64–74 m, respectively.

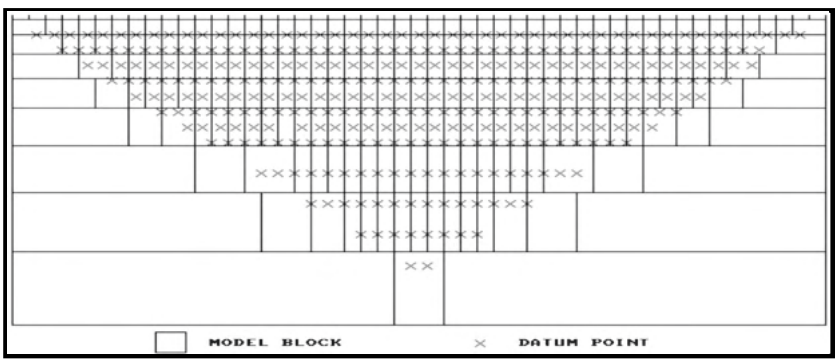

Fig. 7 Arrangement of model blocks and apparent resistivity data points

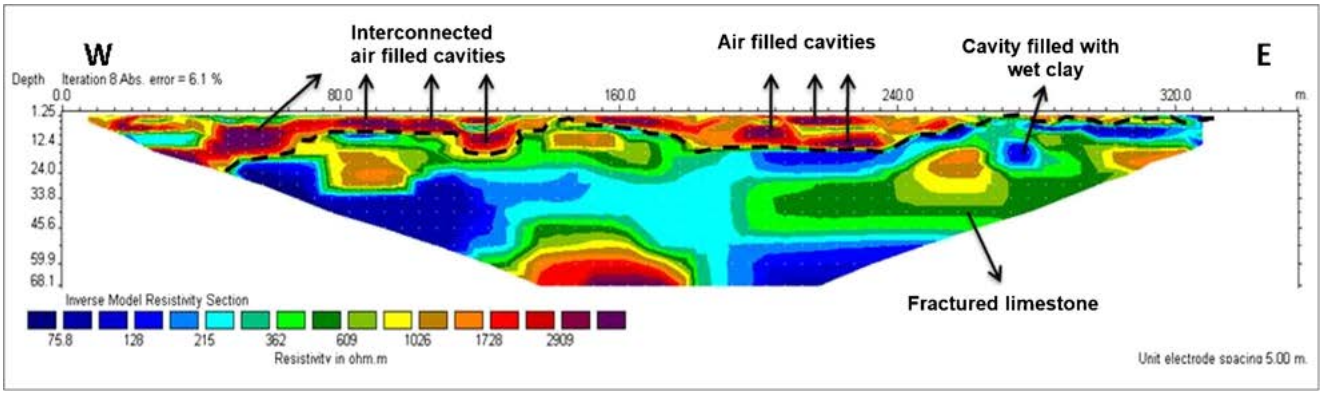

Fig. 8 Interpretation of the Rufa 1 ERT profile

All these events can refer to the occurrence of karst features. The heterogeneity of the subsurface in this profile can be inferred from the dipping reflections plotted as a solid line in the graph.

In the other part of this radiogram (Fig. 11b) at a horizontal distance of 250 m, a small diffraction hyperbola could be interpreted as a small cavity placed near the surface. Another anomaly with nearly the same characteristics is located at a 252 m horizontal distance.

Rufa 3 ERT profile

The electrical resistivity (ER) data in this profile were collected along the SW–SE trending line with a total profile length of 360 m (Fig. 12). A thick zone of the limestone formation with a depth range of 35 m in the SW part of the profile decreasing gradually to the end part of the profile is recognized with low resistivity value. This zone reflects the much fractured limestone

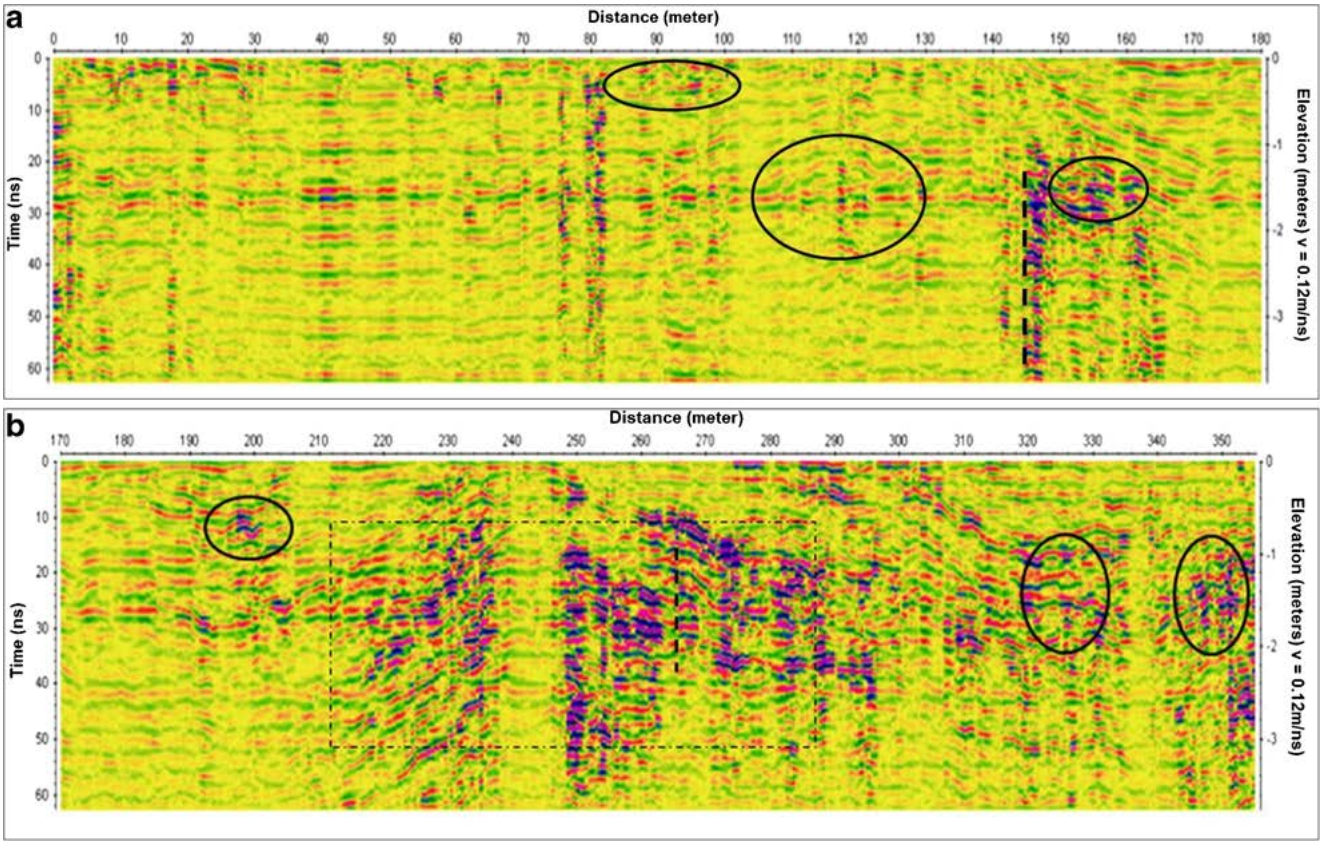

Fig. 9 **a** Part of the GPR profile Rufa 1 from 0 to 180 m. **b** Part of the GPR profile Rufa 1 from 180 m to the end

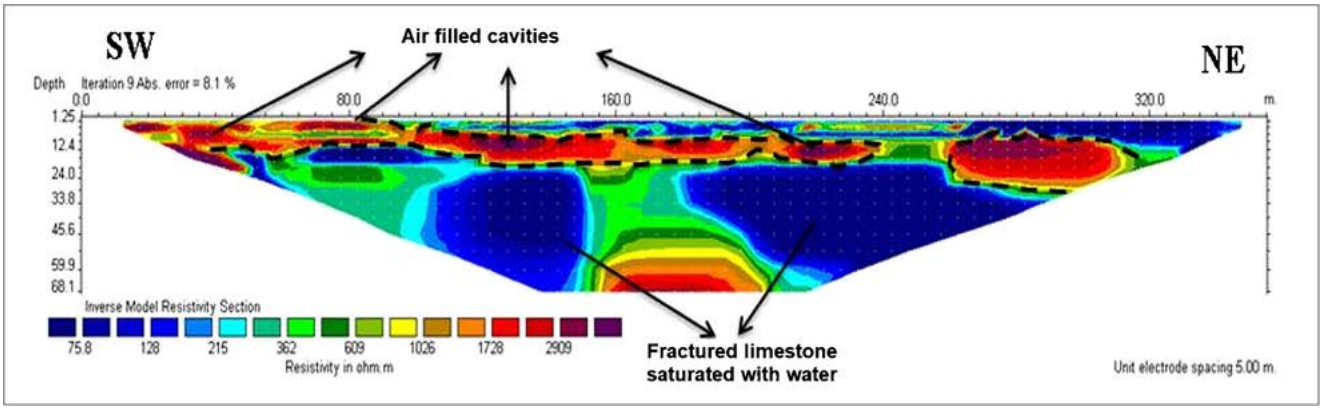

Fig. 10 Interpretation of the Rufa 2 ERT profile

saturated with water. A highly resistive zone exceeding 400 Ω·m comes after this one, representing the bedrock limestone. Through the last zone, an offset placed or located between 138 and 165 m could be determined. This feature may refer to the existence of karst development related to the role of the penetrating groundwater in the process of rock solution.

Rufa 3 GPR profile

This radiogram is measured along the ERT profile Rufa 3 (Fig. 13a, b). Generally speaking, this section is characterized with high-amplitude reflection. The vertical and subvertical fractures are spread along the section. They can be delineated by tracing the discontinuity and displacement of reflection in the

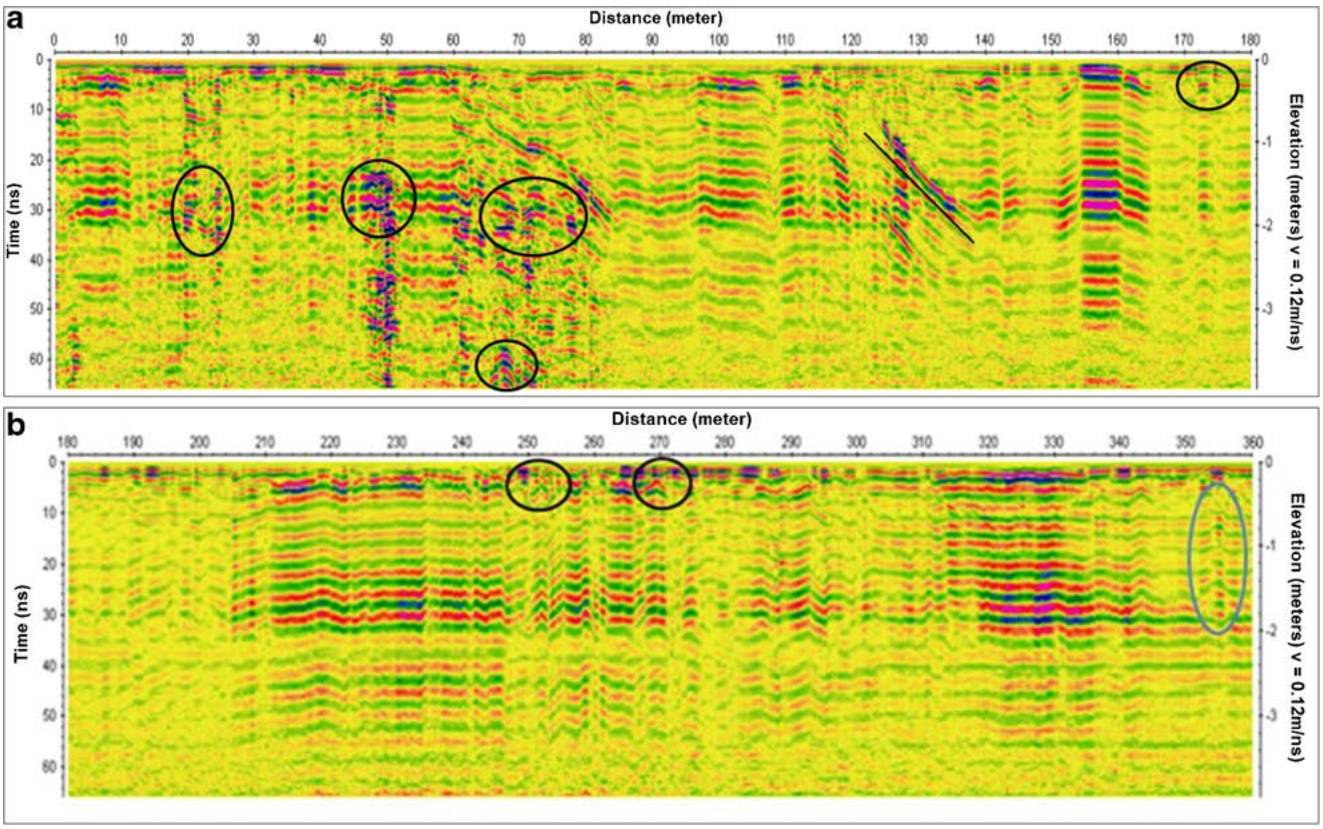

Fig. 11 **a** Part of the GPR profile Rufa 2 from 0 to 180 m. **b** Part of the GPR profile Rufa 2 from 180 m to the end

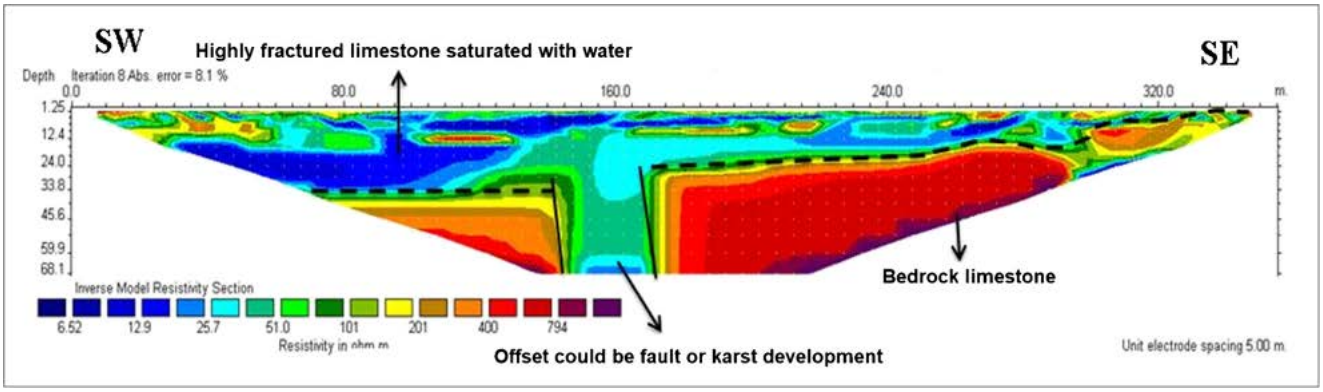

Fig. 12 Interpretation of the Rufa 3 ERT profile

vertical and horizontal directions as shown in a black dashed line in the horizontal distances of 18 m, 30 m, 157 m, and 262 m in (Fig. 13a, b), respectively. All these fractures are located very near from the surface and play as channels for water contributing finally in forming and developing the subsurface cavities.

The other karstic features in this section are represented by cavities in the form of hyperbolas or distortion in reflection signal. This can be seen clearly between 70 and 80 m horizontal distances in Fig. 16 where a cavity is extended from 0.5 m down in the subsurface to nearly 2.4 m. The other one cavity is delineated at 245 m horizontal distance starting 0.2 m and extending down to nearly 1.5 m (Fig. 13b). The distortion and uplift of the reflection events can be at the depth between 1.6 and 2.4 m and horizontal distance between 36 and 50 m as shown in Fig. 13a and at the depth between 1.1 and 2.3 m and horizontal distance between 184 and 196 m as shown in Fig. 13b.

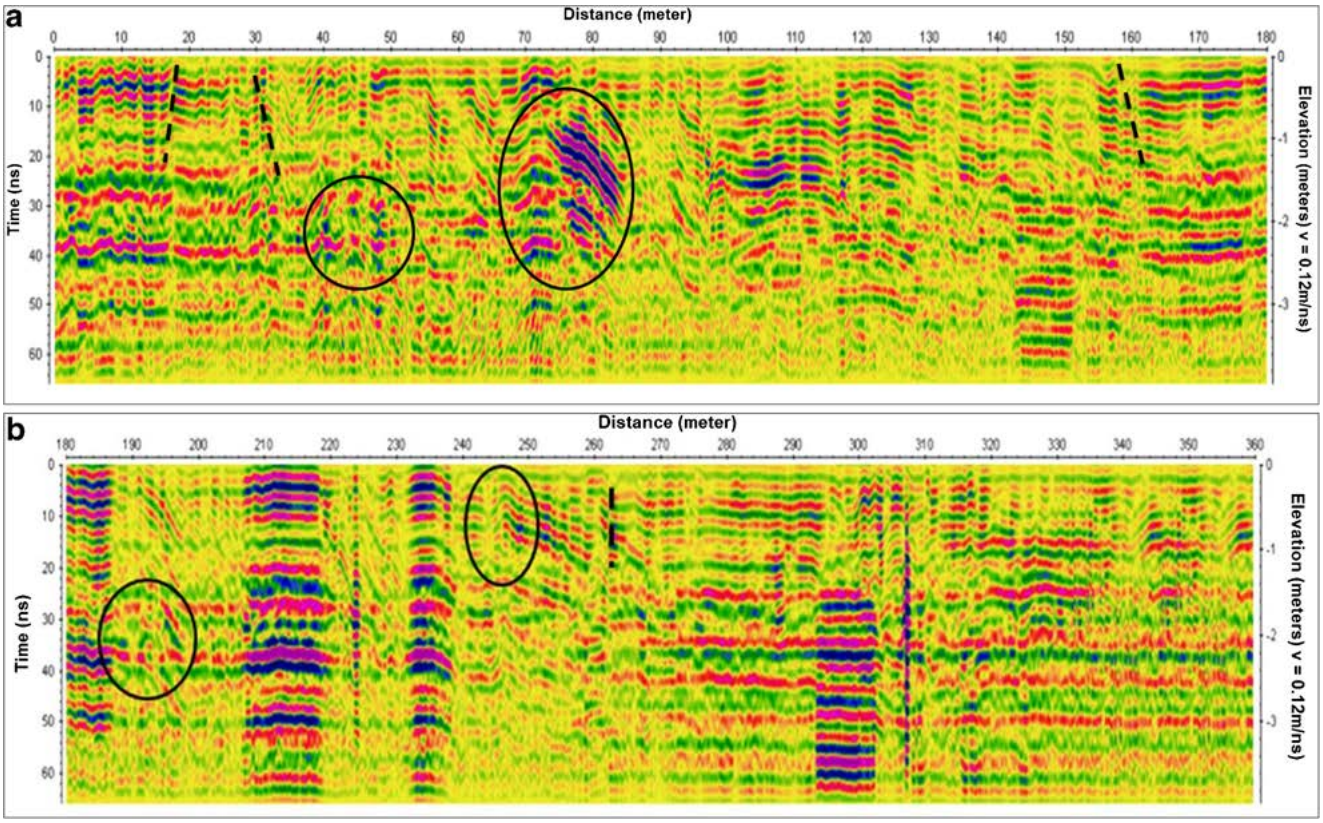

Fig. 13 **a** Part of the GPR profile Rufa 3 from 0 to 180 m. **b** Part of the GPR profile Rufa 3 from 180 m to the end

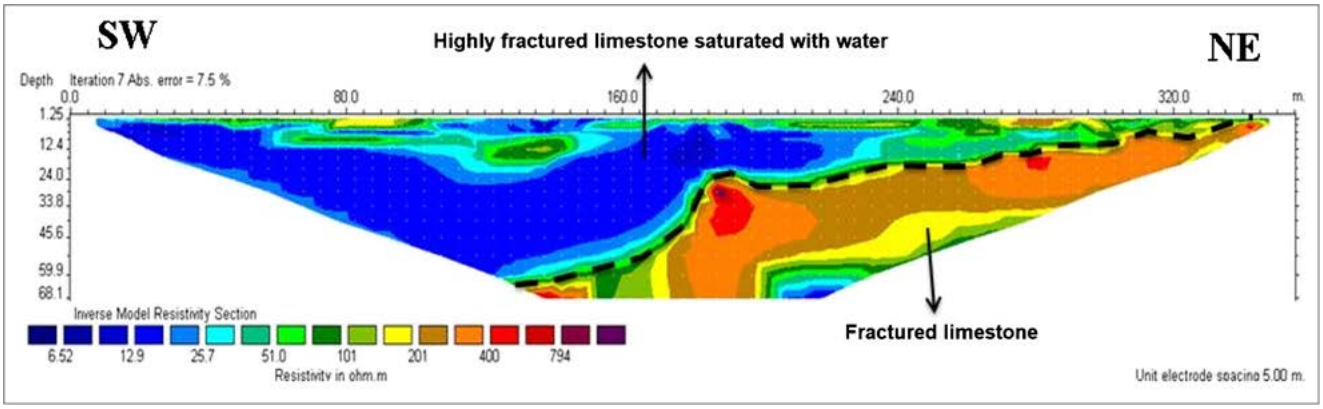

Fig. 14 Interpretation of the Rufa 4 ERT profile

Rufa 4 ERT profile

This line was measured along SW–NE trending. Two different zones in this line could easily be delineated by the black dashed line shown in Fig. 14. The first zone is distinguished by a low resistivity value and characterizes the SW part of the profile. This part reflects the fractured limestone saturated with water as this part can be compared with the end part of profile 2 where they intersect. The second zone has a higher resistivity value indicating the non-saturated fractured limestone.

Rufa 4 GPR profile

This profile was conducted along the ERT profile Rufa 4, but in an opposite direction. In this section, the karstic features can be noticed from discontinuity and lateral variations in reflection events. In the horizontal distance of 10 m and the depth

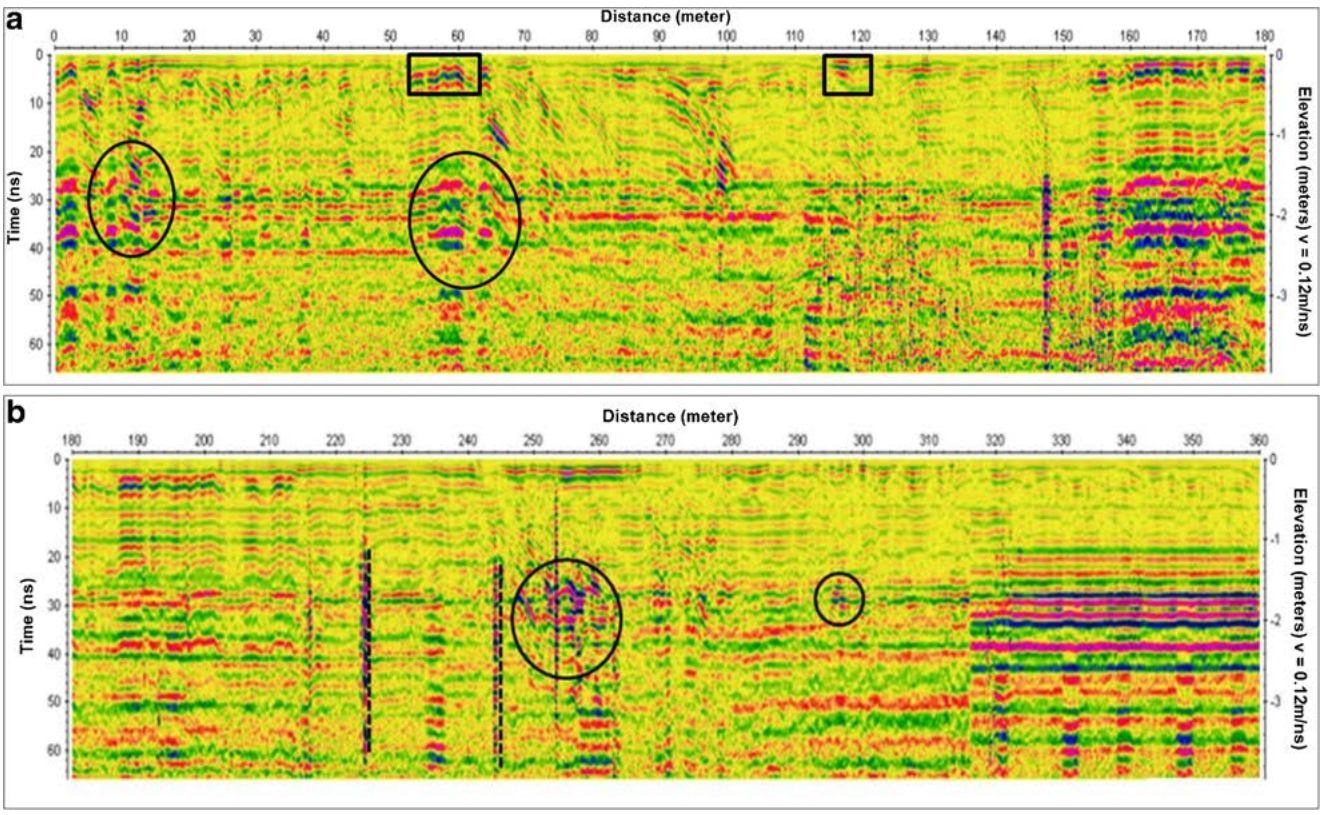

Fig. 15 **a** Part of the GPR profile Rufa 4 from 0 to 180 m. **b** Part of the GPR profile Rufa 4 from 180 m to the end

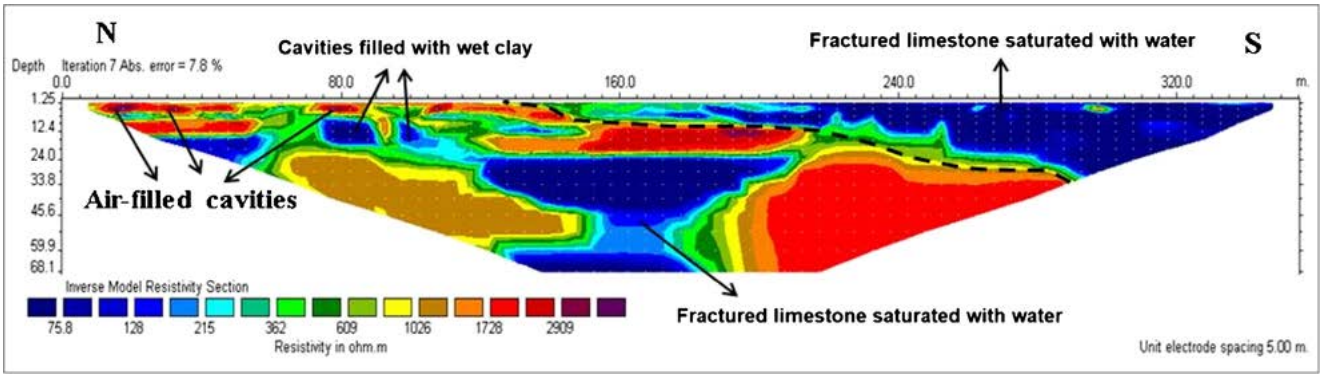

Fig. 16 Interpretation of the Rufa 5 ERT profile

ranging from 1 to 2.2 m, an uplift and lateral discontinuity could be interpreted as a cavity. The same feature is repeated within the horizontal distance of 25–64 m, and a depth extends from 1.2 to 2.3 m (Fig. 18). Another karstic feature can be inferred from the intensity of the strong signal of the reflections located between 250 and 260 m and a depth extension equal to 1.2 m (Fig. 15a).

A vertical repeat of signal diffraction and a cutoff in horizontal reflection could be delineated at 224 m and 243 m horizontal distances, respectively (Fig. 15b). Those two features which are interpreted as the fractured zone appear about 1 m from the surface and extend down in the section.

Rufa 5 ERT profile

It takes the direction from north nearly from the center of the first line to south ending next to the center of profile 3 (Fig. 16). The center of this ERT profile can easily be correlated with the middle part of profile 2 as it crosses through it. The northern part of the profile is characterized by the existence of numerous anomalies within the limestone formation. Between the depths of 2 and 5 m, there exist three high-resistivity anomalies between offsets 13–18 m, 27–34 m, and 75–85 m, respectively. As a rule of thumb, those anomalies reflect

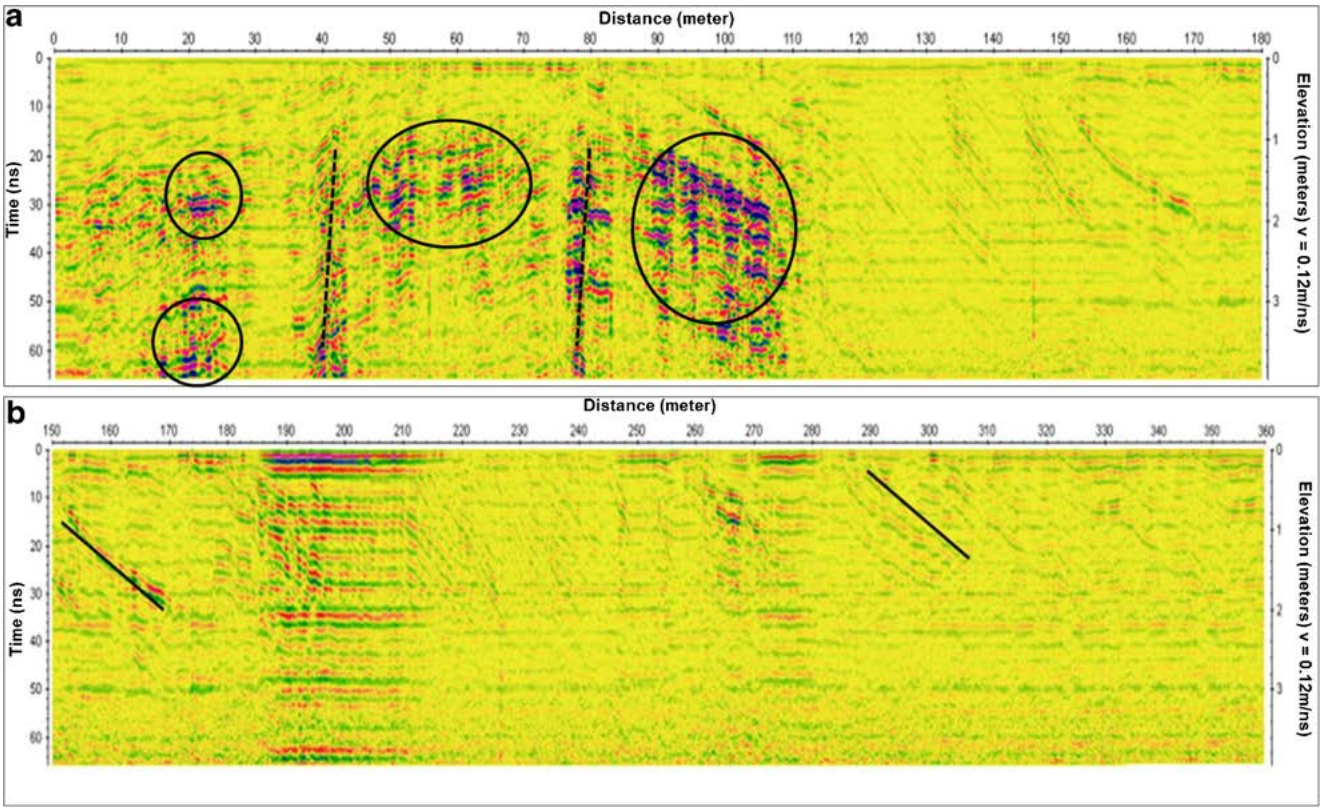

Fig. 17 **a** Part of the GPR profile Rufa 5 from 0 to 180 m. **b** Part of the GPR profile Rufa 5 from 180 m to the end

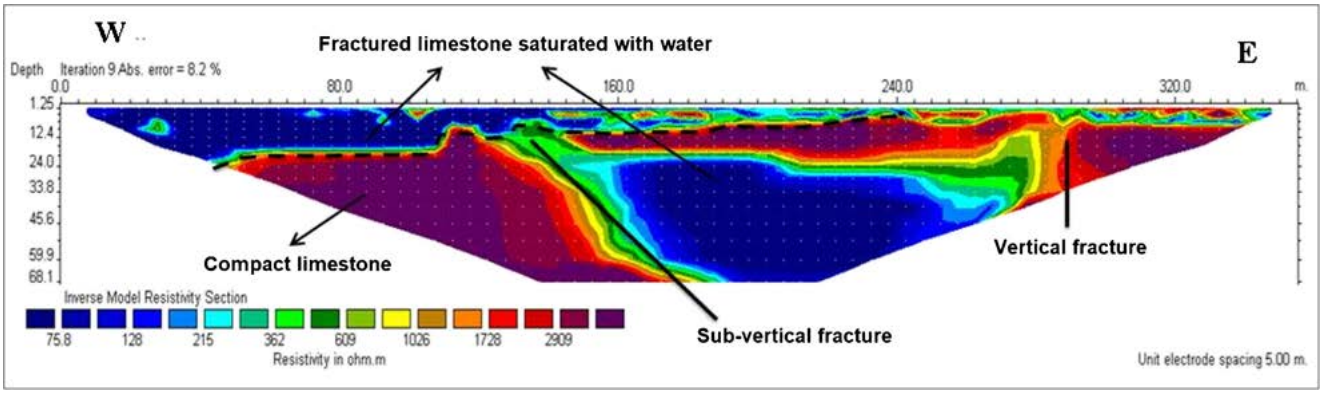

Fig. 18 Interpretation of the Rufa 6 ERT profile

the existence of air-filled cavities. The northern part of the profile is characterized by the existence of numerous anomalies within the limestone formation. Between the depths of 2 and 5 m, there exist three high-resistivity anomalies between offsets 13–18 m, 27–34 m, and 75–85 m, respectively. As a rule of thumb, those anomalies reflect the existence of air-filled cavities. The most upper southern end of the profile approaches the center of profile 3 as the two parts have the same range of the resistivity values indicating the fractured limestone saturated with water.

Rufa 5 GPR profile

This GPR data section was measured in the same direction of resistivity line Rufa 5 (Fig. 17a, b). Most of the karstic features in this radiogram are in relation with the intensity of the strong signal of the reflection events as it can be seen in the horizontal distances 18–24 m, 46–62 m, and 95–108 m which agreed in the depth between 0.9–1.6 m, 0.6–1.8 m, and 1–2.8 m, respectively. A discontinuity in the horizontal direction associated with a displacement is mapped in the horizontal distance 80 m at a depth starting at 1 m and extends to the end of the section.

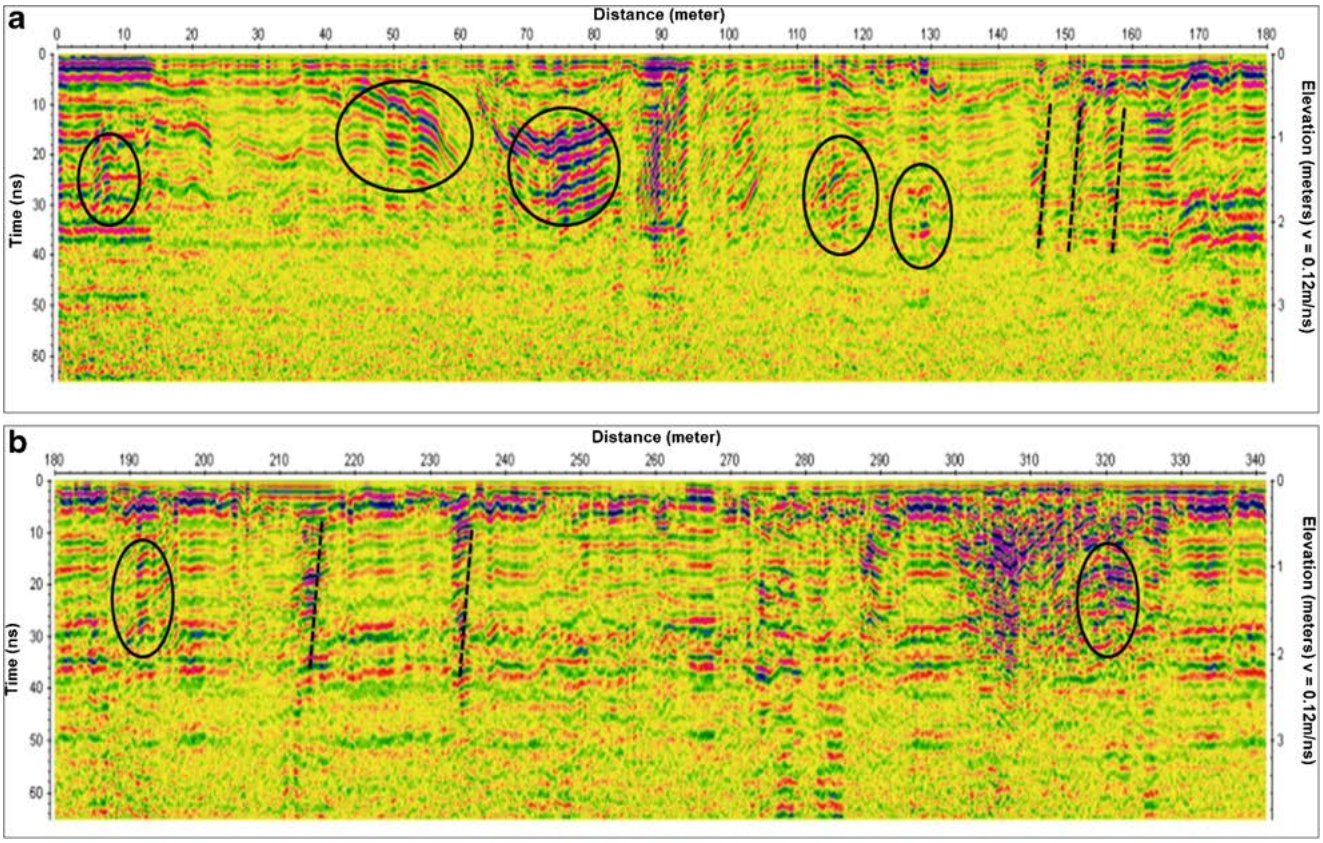

Fig. 19 **a** Part of the GPR profile Rufa 6 from 0 to 180 m. **b** Part of the GPR profile Rufa 6 from 180 m to the end

This may be interpreted as a fracture zone (Fig. 17a). After the horizontal distance 110 m, the section seems to be attenuated as a result of the high moisture in this part of the section which weakens the radar signal.

Rufa 6 ERT profile

This ER line is measured from the west neighbor end of profile 5 to the east direction. A shallow layer of fractured limestone is saturated with water in the western part, decreasing in thickness and percentage of saturation as it moves to the eastern part (Fig. 18). A compacted hard limestone layer is placed under the shallower one. This layer is affected by the existence of two subvertical and vertical fractures located between offsets 115–155 m and 265–290 m, respectively. Those two fractures may clarify the presence of the high-fractured-limestone-saturated-with-water zone located in between them. They can play as channels for the surface water penetrating into the subsurface.

Rufa 6 GPR profile

This profile was measured in the direction from west to east in agreement with ERT profile Rufa 6. The karstic features in this profile appear nearly in the first 2 m of the subsurface while the other part is attenuated. At the beginning of this radiogram, definitely at the horizontal distance of 9 m and depth of 1–1.8 m, hyperbola diffraction is located, referring to a cavity occurrence. Intensity in reflection amplitude is located along the horizontal distance of 24–54 m and 65–80 m in a depth ranging from 0.6 to 1.8 m (Fig. 19a).

In the second part of the section (Fig. 19b), two subvertical parallel fracture zones are delineated at 214 m and 236 m horizontal distances, respectively. A distinct uplift and discontinuity zone could be documented in the horizontal distance of 320 m starting at the 0.9 m depth and extending to nearly 2 m down.

Conclusion

Electrical resistivity tomography and ground-penetrating radar used in this work could be applied successfully to delineate and map the subsurface karstic features like cavities and fractured zones over the Sulaiy Formation in the eastern Rufa Graben. Those karstic features show various sizes and located generally in the shallower part of the profile sections.

The air-filled cavities could be detected and delineated in the interpreted profile sections characterized with high resistivity values in consideration to the whole profile. On the other hand, the non-air-filled cavities which were rare and encountered in Rufa 1 profile and Rufa 5 profile have a low resistivity value.

These distinctive high and low resistivity values referring to the air-filled and water-filled cavities respectively spreading through the study area agreed with relative resistivity values of many published studies around the world such as the studies achieved by Cardarelli et al. (2010), McGrath et al. (2002), Abdeltawab (2013), and Abdallatif et al. (2015).

The cavities and fractures which appeared as a hyperbola in all the six GPR data sections or as amplification associated with uplift or discontinuity of reflection events and linear interface are similar to those documented by Abdeltawab (2013) and Abdallatif et al. (2015).

It can be concluded from this study that the application of electrical resistivity tomography using the dipole–dipole configuration is an effective and useful tool in mapping and delineating karst features in the eastern Rufa Graben. The near-surface cavities were shown and mapped in this method as high-resistivity anomalies interpreted as air-filled cavities in most of the interpreted profiles. The cavities filled with wet clay which are rare in comparison with air-filled cavities appeared as low-resistivity anomalies in the electric section. This method could also give an initial image of the subsurface stratigraphic consequence, depending on dividing the subsurface into different layers with different resistivity values.

The GPR techniques also contributed in mapping and delineating the subsurface cavities and fractured zones in the first 3 m of the subsurface in the study area. This technique could image the karstic features which were not detected by the electric method as a result of the used electrode space.

The results of this study from the two methods confirm the presence of the subsurface karstic features in the sully formation. The mapping of such subsurface karstic features and their distribution will contribute in the future in decreasing the cost of drilling works during any construction foundation.

Funding information This project was supported by the NSTIP strategic technologies program (number 12-WAT-2867-2) in the Kingdom of Saudi Arabia.

References

Abdallatif T, Khafagy A-SA, Khozym A (2015) Geophysical investigation to delineate hazardous cavities in Al-Hassa Karstic Region, Kingdom of Saudi Arabia, in Engineering Geology for Society and Territory Volume 5 Springer. p. 507–514

Abdeltawab S (2013) Karst limestone foundation geotechnical problems, detection and treatment: case studies from Egypt and Saudi Arabia. Int J Sci Eng Res 4(5):376–387

Abu-Shariah MI (2009) Determination of cave geometry by using a geoelectrical resistivity inverse model. Eng Geol 105(3–4):239–244

Amrouche M, Saibi H (2019) Feasibility study of karst feature detection using microgravity data inversion. International Conference on Engineering Geophysics, United Arab Emirates University, Al-Ain, UAE

Carbonel D, Rodríguez-Tribaldos V, Gutiérrez F, Galve JP, Guerrero J, Zarroca M, Roqué C, Linares R, McCalpin JP, Acosta E (2015)

Investigating a damaging buried sinkhole cluster in an urban area (Zaragoza city, NE Spain) integrating multiple techniques: geomorphological surveys, DInSAR, DEMs, GPR, ERT, and trenching. Geomorphology 229:3–16

Cardarelli E, Cercato M, Cerreto A, Di Filippo G (2010) Electrical resistivity and seismic refraction tomography to detect buried cavities. Geophys Prospect 58(4):685–695

Chalikakis K, Plagnes V, Guerin R, Valois R, Bosch FP (2011) Contribution of geophysical methods to karst-system exploration: an overview. Hydrogeol J 19(6):1169

Claerbout JF, Muir F (1973) Robust modeling with erratic data. Geophysics 38(5):826–844

Cook JC (1965) Seismic mapping of underground cavities using reflection amplitudes. Geophysics 30(4):527–538

Daniels DJ (2004) Ground penetrating radar, vol. 1. IEE radar, sonar, navigation, and avionics series

Davis J, Annan A (1989) Ground-penetrating radar for high resolution mapping of soil and rock stratigraphy. Geophys Prospect 37(5):531–551

Deceuster J, Delgranche J, Kaufmann O (2006) 2D cross-borehole resistivity tomographies below foundations as a tool to design proper remedial actions in covered karst. J Appl Geophys 60(1):68–86

Grandjean G, Gourry J-C (1996) GPR data processing for 3D fracture mapping in a marble quarry (Thassos, Greece). J Appl Geophys 36(1):19–30

Grasmueck M (1996) 3-D ground-penetrating radar applied to fracture imaging in gneiss. Geophysics 61(4):1050–1064

Hollingsworth E, Brahana V, Inlander E, Slay M (2008) Karst Regions of the World (KROW): global karst datasets and maps to advance the protection of karst species and habitats worldwide. In: USGS Karst Interest Group Proc., Kentucky, May 27-29, 2008. Ed. E. L. Kuniansky, USGS Scientific Investigations Rep. 2008-5023, p. 17–24

Jado A, Johnson D (1983) Solution caverns in the Dammam Dome, Dhahran, Saudia Arabia. Springer Heidelberg tiergartenstrasse 17, D-69121 Heidelberg, Germany. p. 69–73

Loke MH (2000) Electrical imaging surveys for environmental and engineering studies: a practical guide to 2-D and 3-D surveys. Electronic version available from http://www.terraplus.com

Loke MH (2002) Rapid 2-D Resistivity and IP inversion using the least-squares method, Geoelectrical Imaging 2D and 3D. Geotomo Software.

McGrath R, Styles P, Thomas E, Neale S (2002) Integrated high-resolution geophysical investigations as potential tools for water resource investigations in karst terrain. Environ Geol 42(5):552–557

Metwaly M, AlFouzan F (2013) Application of 2-D geoelectrical resistivity tomography for subsurface cavity detection in the eastern part of Saudi Arabia. Geosci Front 4(4):469–476

Parise M, Gunn J (2007) Natural and anthropogenic hazards in karst areas: recognition, analysis and mitigation. Geological Society of London

Phoenix HC (1985) Interpretation of radiometric data from the cover rocks geophysical survey, in Phoenix Corporation report prepared for U.S. Geological Survey and Saudi Arabian Deputy Ministry for Mineral Resources, Jeddah p. 76p

Powers RW, Ramirez LF, Redmond CD, Elberg EL (1966) Geology of the Arabian Peninsula. Geological survey professional paper. 560: 1–47

Pueyo-Anchuela Ó, Casas-Sainz AM, Soriano MA, Pocoví-Juan A (2010) A geophysical survey routine for the detection of doline areas in the surroundings of Zaragoza (NE Spain). Eng Geol 114(3–4): 382–396

Reynolds JM (2011) An introduction to applied and environmental geophysics. John Wiley & Sons

Saibi H., M. Amrouche (2018) Microgravity inversion for 3D subsurface density modeling of Al-Ain Region, Abu Dhabi, United Arab Emirates. JpGU Annual Meeting 2018, Chiba, Japan

Saibi H, Amrouche M, Fowler A (2019) Deep cavity systems detection in Al-Ain City from gravity surveys inversion. J Asian Earth Sci 182: 103937. https://doi.org/10.1016/j.jseaes.2019.103937

Sandmeier KJ (1998) ReflexW program for the processing of seismic, acoustic or electromagnetic reflection, refraction and transmission data. Sandmeier Software, Karlsruhe

Sum CW, Othman J, Loganathan P (1996) Geotechnical problems in limestone terrain with emphasis on cavities and sinkholes. In Seminar Geologi dan Sekitarn, UKM, Puri Pujangga, Bangi (pp. 102–117)

Takahashi K, Preetz H, Igel J, and Kuroda S (2012) Basics and application of ground-penetrating radar as a tool for monitoring irrigation process. INTECH Open Access

Ulriksen CP (1982) Application of impulse radar to civil engineering. Lund University. Doctoral Thesis

Vaslet D, Al-Muallem M, Maddeh S, Brosse J, Fourniquet J, Breton J, Le Nindre Y (1991) Explanatory notes to the geologic map of the Ar Riyad Quadrangle, sheet 24 I, Kingdom of Saudi Arabia. Saudi Arabian Deputy Ministry for Mineral Resources, Jeddah. Geosciences 121:1–54

Wilson WL, Beck BF (1988) Evaluating sinkhole hazards in mantled karst terrane. In Geotechnical aspects of karst terrain exploration, foundation design and performance, and remedial measures. ASCE

Yassin RR, Muhammad RF, Taib SH, Al-Kouri O (2014) Application of ERT and aerial photographs techniques to identify the consequences of sinkholes hazards in constructing housing complexes sites over karstic carbonate bedrock in Perak, Peninsular Malaysia. J Geogr Geol 6(3):55

Youssef AM, El-Kaliouby HM, Zabramawi YA (2012) Integration of remote sensing and electrical resistivity methods in sinkhole investigation in Saudi Arabia. J Appl Geophys 1(87):28–39

Zhou W, Beck BF, Adams AL (2002) Effective electrode array in mapping karst hazards in electrical resistivity tomography. Environ Geol 42(8):922–928